Title: Activated regulatory T-cells, dysfunctional and senescent T-cells dominate the microenvironment of pancreatic cancer

Authors: Shivan Sivakumar[1,2,3†], Enas Abu-Shah[2,4†*], David J Ahern[2], Edward H Arbe-Barnes[5], Nagina Mangal[6], Srikanth Reddy[3], Aniko Rendek[3], Alistair Easton[1], Elke Kurz[2], Michael Silva[3], Zahir Soonawalla[3], Lara R Heij[7,8], Rachael Bashford- Rogers[9], Mark R Middleton[1,3‡], Michael L Dustin[2‡*]

Affiliations:

[1] Department of Oncology, University of Oxford, Oxford OX3 7DQ, UK. [2] Kennedy Institute of Rheumatology, University of Oxford, Oxford OX3 7FY, UK. [3] Oxford University Hospitals NHS Foundation Trust, Oxford, UK. [4] Sir William Dunn School of Pathology, University of Oxford, Oxford OX1 3RE, UK. [5] University of Oxford Medical School. [6] Nuffield Department of Surgical Sciences, University of Oxford, Oxford OX3 9DU, UK. [7] Department of General, Gastrointestinal, Hepatobiliary and Transplant Surgery, RWTH Aachen University Hospital, Aachen Germany. [8] Institute of Pathology, University Hospital RWTH Aachen, Aachen, Germany. [9] Wellcome Trust Centre for Human Genomics, University of Oxford, Oxford OX3 7BN, UK.

† These authors contributed equally to the work.
‡ These authors jointly directed the work.
* correspondence should be addressed to: enas.abushah@path.ox.ac.uk, or michael.dustin@kennedy.ox.ac.uk

Abstract:

Pancreatic cancer has the worst prognosis of any human malignancy and leukocyte infiltration is a major prognostic marker of the disease. As current immunotherapies confer negligible survival benefits, there is a need to better characterise leukocytes in pancreatic cancer to identify better therapeutic strategies.

In this study, we analysed 32 human pancreatic cancer patients from two independent cohorts. A multi-parameter mass-cytometry analysis was performed on 32,000 T-cells from eight patients. Single-cell RNA sequencing dataset analysis was performed on a cohort of 24 patients. Multiplex immunohistochemistry imaging and spatial analysis were performed to map immune infiltration into the tumour microenvironment.

Regulatory T-cell populations demonstrated highly immunosuppressive states with high TIGIT, ICOS and CD39 expression. $CD8^+$ T-cells were found to be either in senescence or an exhausted state. The exhausted CD8 T-cells had low PD-1 expression but high TIGIT and CD39 expression. These findings were corroborated in an independent pancreatic cancer single-cell RNA dataset from additional 24 patients.

These data suggest that T-cells are major players in the suppressive microenvironment of pancreatic cancer. Our work identifies novel therapeutic targets that should form the basis for rational design of a new generation of clinical trials in pancreatic ductal adenocarcinoma.

Introduction

Pancreatic ductal adenocarcinoma (PDAC) has the worst outcomes of any human cancer with a 5-year survival around 7% (*1*). Early diagnosis with surgical resection followed by combination chemotherapy offers the best chance of long-term survival (*2*). We and others have shown that the immune infiltrate in the primary pancreatic tumour is prognostic of the clinical course after a surgical resection (*3, 4*). Pancreatic cancer has a complex immune microenvironment with T-cells, macrophages, neutrophils, NK cells, B-cells and dendritic cells present (*5-9*). Checkpoint blockade immunotherapies, especially antibodies to PD-1 and PD-L1, reactivate tumour-specific T-cells and have demonstrably improved the prognosis of melanoma and lung cancer (*10, 11*). However, these immunotherapies have had minimal effects on outcomes in pancreatic cancer, with no durable responses in patients (*12-15*).

Due to the poor response of checkpoint blockade agents in PDAC, we propose taking a step back and characterise the states and specific populations of T-cells in this disease, which is the focus of this paper. Although it has been shown that $CD4^+$, $CD8^+$ and regulatory T-cells (Tregs) infiltrate the microenvironment of PDAC, little is known about their phenotype, differentiation or activation status (*16, 17*). Furthermore, although cancer therapeutics has been dominated by PD-1 and CTLA-4 targeting antibodies, many other checkpoints with the potential to impinge on the clinical course of PDAC, including TIGIT, Tim3, Lag3 and CD39, have been identified. Co-stimulatory molecules; which promote suppressive function of $CD4^+$ regulatory T cells and $CD8^+$ suppressor cells, such as ICOS, OX40, CD40L, GITR and 4-1BB may also bear upon outcomes (*18, 19*).

In this study we characterised the immune landscape in primary tumours and the periphery of patients with pancreatic cancer, focusing on T-cells' functional states, and their immune checkpoint expression patterns.

Results

Heterogenous and suppressive innate immune cell composition within pancreatic cancer

Using fresh samples from tumour resections (Table 1) and matched blood samples, we identified the main cellular components and immune lineages with a panel of mass-cytometry (CyTOF) antibodies (Fig. 1a, Table 2). The epithelial cell content of samples was 25.81±6.92% (median±sd) and that of the stroma 50.06±14.66% (Fig.1b), in agreement with the highly fibrotic nature of PDAC (*20*). All 8 patients exhibited a significant level of immune cell involvement, with $CD45^+$ being 22.85±12.60% of all live cells (Figure 1- figure supplement 1).

We identified the main immune cell lineages illustrated in the viSNE plot and marker expression maps (Fig. 1c). We further characterised different metaclusters of cells corresponding to different lineages using unsupervised hierarchical clustering (Fig. 1d; coloured viSNE and heatmap). There were multiple shared features across all patients including the presence of $CD4^+$ T-cells (metacluster 11), $CD8^+$ T-cells (metacluster 7), granulocytes (metaclusters 8,10) and mononuclear phagocytes (metaclusters 1,2) and myeloid-derived suppressor cells (MDSCs; metaclusters 4,5). Interestingly, both B-cells (metacluster 3) and NK cells (metacluster 9) numbers were negligible (<0.5%) in some patients' tumours (Fig. 1d, inset). For example, the tumour

in patient 3 was deficient in B-cells and that in patient 8 deficient in NK cells (Fig. S2b).

We identified multiple subsets of NK cells (Fig. 1e, Figure 1- figure supplement 3), granulocytes (Fig. 1f, Figure 1- figure supplement 3) and mononuclear phagocytes (Fig. 1g, Figure 1- figure supplement 4). Strikingly, most NK metaclusters expressed the inhibitory molecule TIGIT, with those having the highest expression being granzyme B (GzmB) negative, indicative of defective cytotoxicity (e.g metacluster 7). These cells also exhibited tissue residency features, such as expression of the adhesion molecule CD103. Conversely, the infiltrating NK populations had features of cytotoxicity with CD16, CD57 and GzmB expression (metaclusters 4,6).

The majority of the granulocytes were $CD15^{+}CD16^{+}CD14^{\pm}$, corresponding with granulocyte-MDSCs (G-MDSC) (*21, 22*) or antigen-presenting tumour associated neutrophils (*23*), marked by their HLA-DR expression (metacluster 4), although we also observed the co-expression of PD-L1.

In the myeloid compartment, we identified MDSCs expressing low levels of HLA-DR and high PD-L1 (metaclusters 3), and G-MDSC (metacluster 6). The majority of myeloid cells had an intact antigen presentation capability marked by high levels of HLAD-DR (metaclusters 2,4,5). This is in contrast to previous reports describing the major myeloid infiltration in PDAC to be MDSCs (*21, 24*).

Peripheral blood from the same patients presented different population compositions (Figure 1- figure supplement 5). Specifically, we observed a small percentage (1.26±1.37%) of low-density neutrophils in the PBMC samples (Figure 1- figure supplement 5a, metacluster 11,14) which have been described in PBMCs of patients with tumours (*25*). Circulating NK cells, unlike the tumour-associated NK cells, appeared to retain their cytolytic activity with most sub-populations expressing $CD56^{dim}$, CD57, GzmB and CD16 (Figure 1- figure supplement 5b). We also observed a significant population of circulating MDSCs (Figure 1- figure supplement 5a, metacluster 3, 27.82±8.09%) and the presence of T-cell/monocyte conjugates (Figure 1- figure supplement 5a, metaclusters 2 and 13, 0.85±0.42%) expressing PD-L1 (Figure 1- figure supplement 5c, metacluster 1) suggestive of an immune perturbation (*26*) (Figure 1- figure supplement 5c, metacluster 1).

Suppressive and non-tumour responsive T-cells predominate PDAC microenvironment

We hypothesised that the lack of activity of established checkpoint inhibitors such as anti CTLA-4 and anti PD-1 indicates they are not prominent pathways in PDAC. To test this hypothesis, we re-evaluated T-cells' states in the tumour microenvironment. We analysed the $CD3^+$ T-cells functional states from PDAC tumours using differentiation,activation and checkpoint markers, to characterise the $CD8^+$ (Fig. 2a, Figure 2- figure supplement 1), $CD4^+$ (Fig. 2b, Figure 2- figure supplement 2) and Treg (Fig. 2c, Figure 2- figure supplement 3) compartments.

We identified 30 distinct metaclusters of $CD8^+$ T-cells. Multiple metaclusters displayed characteristics of a senescent population, $CD57^+CD27^-CD28^-$ (metaclusters 5,11; 3.89±3.66% of $CD8^+$ T cells) or terminally differentiated $CD45RA^+CD27^{-/low}CD28^{-/low}$ (metaclusters 2,7,8; 40.57±18.06%). These cells have been previously described in the context of aging and viral infections and are associated with proliferative senescence and reduced T-cell signalling, whilst maintaining their cytolytic capabilities (*27-29*). More recently, these have been observed in the context of cancer (*30, 31*), however, this is the first report to describe them in pancreatic cancer. Two suppressive populations with negative immune modulatory effects were identified: (i) a metacluster of $FoxP3^+$ $CD8^+$ "regulatory" T-cells (metacluster 12), which was only present in 2 out of the 8 patients (Figure 2- figure supplement 1), and (ii) an exhausted population expressing high levels of multiple inhibitory receptors (metacluster 6; 4.81±8.73%). Interestingly, the exhausted metaclusters exhibited intermediate-low PD-1 expression, which may explain the limited clinical success targeting the PD1-PDL1 axis. We also identified metaclusters with markers of activation (metaclusters 10,13), proliferation and cytotoxicity (metacluster 9). Overall, we determined that ~ 11.63±8.32% (mean±s.d) of the $CD8^+$ T-cells comprise expression profiles potentiating anti-tumour responses while the majority are either unresponsive (naïve, senescent or exhausted) or even inhibitory. This suggests a certain degree of anti-tumour potential of the $CD8^+$ compartment that could be inhibited by other factors preventing the control of the disease.

We next analysed the contribution from $CD4^+$ T-cells as potential mediators to support $CD8^+$ T-cells (Fig. 2b, Figure 2- figure supplement 2). The 10 identified metaclusters were divided into three main groups: (i) senescent and terminally differentiated (metaclusters 6,8,4) or non-tumour responsive (metaclusters 2,5,9,10) (~76.15±9.45%), (ii) exhausted (metacluster 7; 2.71±2.03%) and (iii) $Foxp3^+$

regulatory (~18.53±8.78%). Indeed, the regulatory $CD4^+$ cells comprised between 8.30 and 32.50% of the $CD4^+$ population across patients.

We hypothesised that the Treg population could contribute to inhibiting $CD8^+$ T-cell responses. We characterised the precise Treg states within the tumour microenvironment (Fig. 2c, Figure 2- figure supplement 3). The majority of the Tregs (~54.47±19.15%) showed evidence of functional activation and high suppression capacity. They expressed the TNF superfamily receptor 4-1BB, HLA-DR and the inhibitory receptors PD-1 and TIGIT. Some metaclusters showed evidence of cytotoxic activity ($CD57^+$, metacluster 2) while the most frequent metaclusters had high expression of TIGIT, ICOS and CD39, indicative of potent inhibitory function (*32-36*).

The peripheral blood $CD8^+$ and $CD4^+$ T-cells also exhibited a population of senescent T cells (Figure 2- figure supplement 4a, metacluster 4, 26.02±18.62% of $CD8^+$, Figure 2- figure supplement 4b, metacluster 1, 5.21±10.56% of $CD4^+$), which might reflect the age of our cohort (median 71 years). Both populations had functionally active subsets; in $CD8^+$ an activated and proliferating metacluster was identified ($4\text{-}1BB^+HLADR^+$, metaclusters 7,8, 1.12±0.70%). However, there were no exhausted $TIGIT^+$ $CD8^+$ T-cells in the periphery (Figure 2- figure supplement 5a). There was also a population of cytotoxic $CD4^+$ T-cells ($GzmB^+$, metaclusters 2,7, 2.61±4.05 %). T-cell/monocyte conjugates, were only observed with $CD4^+$ but not $CD8^+$ T-cells ($CD3^+CD4^+CD14^+$, Figure 2- figure supplement 4b, metacluster 11). Finally, the Tregs in the periphery compromised 9.59±4.30% of the $CD4^+$ T-cells, were characterised by high levels of TIGIT expression albeit at lower levels compared to their tumour-associated counterparts (~30% higher median expression, Figure 2- figure supplement 5b). Not surprisingly, there was a larger naïve population ($CCR7^+CD45RA^+$) compared to the tumour, 13.2±5.47% vs 6.56±3.75%.

Single-cell RNA sequencing validates senescence and regulatory signatures in tumour infiltrating T-cells

The CyTOF analysis highlighted senescent T-cells and $TIGIT^+ICOS^+$ Tregs as potentially important immune cells in pancreatic cancer. We hypothesised similar signatures should be identified on the transcriptional level. We have re-analysed a publicly available single-cell RNA sequencing dataset of 24 PDAC patients from Peng et al (*37*) (Fig. 3). Focusing on the T-cell compartment, we identified 250 unique

clusters as shown in the UMAP (Figure 2- figure supplement 5c, Fig. 3a) corresponding to $CD8^+$ and $CD4^+$ T-cells as well as non-conventional T-cells.

Among those clusters we identified 13 Treg clusters based on *FOXP3* expression, all of which exhibit high expression levels of *TIGIT* and co-expressing *ICOS* and *ENTPD-1* (CD39) (Fig. 3b, violin plots, supplemental data 1). We also identified 6 clusters of senescent T-cells (Fig. 3c) characterised by increased NK marker expression (*KLRG1, KLRB1*) and senescent markers (*HCST*, *HMGB1*) (*28*). Complete differential expression analysis of those populations relative to other $CD4^+$ and $CD8^+$ T-cells is provided in supplemental data 2.

Finally, we also identified exhausted cells characterised by the co-expression of at least 3 of the known exhaustion signature genes *PDCD1, HAVCR2* (Tim-3)*, LAG3, TIGIT, CTLA4 and ENTPD-1*, (Fig. 3d). This has captured exhausted clusters with low *PDCD1* expression (Fig. 3d violin plot clusters 35, 85, 96, 161). Interestingly, previously reported exhaustion genes such as *TOX* (*38*), *LAYN* and *MIR155HC* (*39*), were only upregulated in a subset of the exhausted cell clusters. Together, this suggests a unique exhaustion signature in PDAC-associated T cells.

In summary, we were able to corroborate our observations from the mass cytometry analysis in an independent cohort of PDAC patients at the transcriptomic level. The relative abundance of the T-cell populations identified was similar across the two cohorts (Figure 2- figure supplement 5d).

Effector T-cells are uniformly distributed within pancreatic tumour and Tregs are restricted to the stroma

To investigate the potential cell-cell communication between different T-cell subsets and the surrounding malignant epithelium of the tumour, we analysed cellular spatial distribution using multiplex immunofluorescence (IF) on formalin-fixed paraffin-embedded (FFPE) sections from the same patients as analysed by CyTOF (Fig. 4). For each case we identified cancerous, inflamed (pancreatitis) and normal tissue regions, where available (Fig. 4a-c respectively) and annotated the sub-regions into epithelium (based on pan-Cytokeratin staining) and stroma (based on αSMA staining). Using the expression of the canonical T-cell markers ($CD3^+$, $CD4^+$, $CD8^+$ and $Foxp3^+$), we identified their respective cellular subsets (Figure 4- figure supplement 1). The $CD4^+$ and $CD8^+$ distribution within the different regions of the tissue (Fig. 4d) was

homogeneous with no signs of exclusion from the tumour parencyhma or different stroma regions (Figure 4- figure supplement 1b). Conversely, Tregs were exclusively restricted to the stroma in the cancer and inflamed tissue and almost absent from the epithelium regions. Explaining some recent reports linking Treg depletion to fibroblast pathology in PDAC (*40, 41*). To further elucidate the relationships between the cells we performed proximity analysis (See methods for details) that revealed the majority of $CD8^+$ T-cells to be within 50 μm of the epithelium, with a trend of lower numbers within the cancer region compared to normal albeit not statistically significant (Fig. 4e, $p=0.1167$). 90% of Tregs were in close proximity of a $CD8^+$ T-cell, potentially facilitating their immunosuppressive activity across all assessed regions (Fig. 4f).

Discussion

Here we report one of the first comprehensive characterisation of T-cells in primary human pancreatic ductal adenocarcinoma, revealing multiple distinct immune cell signatures of this tumour with potential for informing therapeutic approaches. Previous reports implied the presence of an immunosuppressive tumour microenvironment, but they lacked a clear definition of its components (*15, 42*) . Here we identify the different immune cells contributing to this phenotype which include granulocytes and myeloid MDSCs (Figure 1), dysfunctional NK cells and T-cells, and regulatory T-cells (Figure 2).

We identified clear signatures of dysfunctional effector T-cell populations which are present in both the $CD8^+$ and $CD4^+$ compartments. The first is an exhausted signature, which surprisingly, is not characterised by the traditional high PD-1 expression, nor does the microenvironment show high expression of its ligand PD-L1 (Fig. S10e). However, exhausted cells express a different set of inhibitory molecules including TIGIT (*43*) and CD39 (Figure 2a, Figure 3c). This finding has a direct implication to designing immune-checkpoint trials where we suspect anti PD-1 combinations might have limited, if any, advantage.

Tregs have been shown to be present in the PDAC microenvironment (*5*), but their functional characteristics are poorly understood. We identified different subtypes of Tregs associated with PDAC, including a highly suppressive Treg population expressing the inhibitory molecule TIGIT and co-stimulatory molecule ICOS (Figure 2c, Figure 3b) whose substantial suppression capacity has been demonstrated by

multiple groups (*32, 34, 44*). There are currently multiple antibodies in development targeting the checkpoint molecules we observed on dysfunctional $CD8^+$ T-cells and Tregs and our data calls for trialling them in PDAC. Specifically, anti-TIGIT has been recently proposed as an alternative immunotherapy to anti PD-1 in colorectal, lung and pancreatic cancers (*45*). From our data we can envision it having an effect not only on dysfunctional $CD8^+$ T-cells but also on NK cells and Tregs.

The spatial analysis of cell distribution in the tumour has revealed a unique localisation of Tregs to the stroma (Figure 4d). These observations, in light of a recent study in a murine model of PDAC that showed depletion of Tregs to result in disease worsening through an increase in pathogenic fibroblasts (*46*), highlight the need to understand the details of Treg/fibroblast interactions and its role in disease progression. A possible strategy proposed from this work would be to block exclusively the activity of the $ICOS^+TIGIT^+$ Tregs population while forgoing any depletion approaches that might result in severe adverse effects.

Finally, we identified a novel senescence signature, which unlike the exhausted phenotype cannot benefit from checkpoint blockade approaches. T-cell senescence has been discussed in the context of viral infections, aging and CAR T-cell therapies and different avenues to replace or rejuvenate those cells through metabolic manipulations, cell therapy and engineering are being investigated (*47-49*). It would be interesting to understand the mechanism of the observed senescence and whether it is directly linked to the immunosuppressive activity of Tregs in the tumour microenvironment (*50, 51*) or related to aging in those patients. If the former, we anticipate that lifting Treg suppression will reverse the phenotype while the latter would require interventions to rejuvenate the cells to increase the chances to elicit anti-tumour responses.

We described features shared between the tumour and the peripheral blood (Figure 1- figure supplement 5, Figure 2- figure supplement 2), especially the circulating $TIGIT^+ICOS^+$ Tregs. Those observations made in patients with localised disease raise the possibility of early detection strategies that warrant investigation in larger cohorts.

In summary, our data maps the T-cell landscape of pancreatic cancer and we propose multiple novel therapeutic approaches to employ immunotherapies in this recalcitrant disease as well as further scientific investigation. Current pancreatic cancer mouse models appear to lack the immune features we observe using human patient

samples (*52*) highlighting the need to directly test the hypotheses generated from this study and its implication through the design of novel clinical trials.

Materials and Methods

Patient recruitment

Samples were collected from 8 patients diagnosed with pancreatic adenocarcinoma (Table 1) that were fit for palliative operation. The 8 patients consisted of 5 males and 3 females and ranged from ages of 51 to 80. 7 out of 8 patients has adjuvant chemotherapy following the operation, patient 2 and 3 have died within 9 months of the operation while patients 4, 6 and 7 have recurred since. All patients were consented for this study via the Oxford Radcliffe biobank (09/H0606/5+5, project: 18/A031).

Sample Collection

From the patients described above, 20 ml blood was collected immediately before surgery into sodium heparin tubes (BD). Tissue samples were placed in RPMI media (Corning) on ice and were reviewed by a designated histopathologist who provided a 10mm by 10mm by 3mm piece for this study. Samples were digested, stained and run on CyTOF.

PBMC Isolation

Blood samples were processed within 4 h of collection. 20 ml of 2% FBS/PBS was added to 20 ml of whole blood. This was layered onto Ficoll-Paque. Sample was centrifuged at 1300 x *g* for 20 min at the slowest acceleration and with break off. After centrifugation, the PBMC ring was removed using a pipette. The ring was topped up with 2% FBS/PBS and centrifuged again at 300 x *g*. Any excess red blood cells were lysed with ACK solution (Life Technologies, A1049201) and cells were washed again.

Tissue Digestion

Sample was initially mechanically disrupted using a scalpel into small pieces. The pieces were put into a 15 ml conical tube, with 9 ml of complete RMPI (10% FBS, 1% Pen/Strep and 1 mM Glutamine) and 1 ml of 10X hyaluronidase/collagenase solution (StemCell, 07912). A first round of digestion was done at 37 ^{o}C for 30 min in a pre-

warmed shaker. The supernatant was collected without disrupting the tissue and a fresh digestion media was added (10 ml complete RPMI containing 200 U of collagenase IV (Lorne Laboratories, LS004194), 100 µl/ml of DNAaseI (Sigma, DN25) and 0.5 U of universal nuclease (Pierce, 88702) for an additional 30 min of digestion as before. The supernatant was combined with the one from the first digestion step and the remaining tumour pieces were squeezed through a 100 µm tissue strainer with a further 10 ml of complete RPMI. The supernatants from all digestion steps were combined and centrifuged for 10 min at 300 x *g*. Any residual red blood cells were removed with ACK solution.

CyTOF sample preparation

Samples were directly taken following isolation for CyTOF staining. Preconjugated antibodies were obtained from Fluidigm or purified antibodies from Biolegend were conjugated in house using Maxpar Conjugation kits (Fluidigm). CD14-Qdot655 was purchased from Thermofisher and acquired in the 114Cd channel - See table 2 for detailed list of antibodies and clones. Cells were incubated with Intercalator-^{103}Rh (Fluidigm, 201103A) for dead cell exclusion, for 10 min at room temperature, followed by staining for surface markers for 20 min at room temperature. Cell fixation and permeabilization was performed using the Foxp3+/Transcription factor staining set (eBioscience, 00-5523-00). The nuclear staining protocol was used for the simultaneous detection of cytoplasmic and nuclear targets (Ki67, CTLA-4, granzyme B and Foxp3), staining was done for 20 min at room temperature. An additional fixation step with 1.6% paraformaldehyde diluted in PBS for 10 min at room temperature. The cells were washed and incubated with 0.125 nM Intercalator-191Ir (Fluidigm, 201192A) diluted in Maxpar fix and perm buffer overnight at 4 ^{o}C until acquisition.

CyTOF Data Acquisition

Immediately prior to acquisition, samples were washed twice with Maxpar cell staining buffer (Fluidigm), twice with cell acquisition solution (Fluidigm) and then resuspended at a concentration of 0.5 million cells/ml in cell acquisition solution containing a 1/10 dilution of EQ 4 Element Beads (Fluidigm, 201078). The samples were acquired on a CyTOF Helios mass cytometer at an event rate of <300 events/second. After acquisition, the data were normalized using bead-based normalization in the CyTOF

software. Data were exported as FCS files for downstream analysis. The data were gated to exclude residual normalization beads, debris, dead cells and doublets, leaving DNA^{+} Rh^{low} events for subsequent clustering and high dimensional analyses.

CyTOF Data Analysis:

Dimensionality reduction visualisation with viSNE and clustering with FlowSOM were done using built in functions in cytobank (https://www.cytobank.org). The number of clusters and metaclusters for the FlowSOM algorithm were reviewed by the researchers. Data was initially overclusterd to identify small populations (all data shown in supplementary figures), but for clarity metaclusters were manually combined following researchers' evaluation and presented in main figures. Heatmaps of normalized marker expression, relative marker expression, and relative difference of population frequency were generated by cytobank and plotted using Prism (GraphPad). Dendograms showing hierarchical clustering of the heatmaps was performed using Morpheus from the Broad Institute (https://www.broadinstitute.org/cancer/software/morpheus/), as an average with 1-Pearson correlation as a parameter.

Collection of Histological Sections

Sections were cut on a Leica RM2235 at around 5 microns thickness, floated on a warm water bath, dissected using forceps to isolate the region of interest and lifted centrally onto TOMO slides (VWR, TOMO® 631-1128). Sections were air-dried. Samples were sequentially labelled with CD4, CD8, Foxp3, Pan Cytokeratin, and αSMA.

Multiplex immunohistochemistry

Multiplex (MP) immunofluorescence (IF) staining was carried out on 4um thick formalin fixed paraffin embedded (FFPE) sections using the OPAL™ protocol (AKOYA Biosciences) on the Leica BOND RXm autostainer (Leica, Microsystems). Six consecutive staining cycles were performed using the following 1ry Antibody-Opal fluorophore pairings: CD4 (clone 4B12, NCL-L-CD4-368 (Leica Novocastra) – Opal 520); CD8 (clone C8/144B, M7103 (DAKO Agilent) -Opal 570); CD3 (clone LN10, NCL-L-CD3-565 (Leica Novocastra) – Opal 540); FOXP3 (clone 236A/E7, ab20034

(Abcam) – Opal 620); Pan Cytokeratin (clone AE1/AE3, M3515 (DAKO Agilent) – Opal 650) and αSMA (rabbit polyclonal, ab5694 (Abcam) -Opal 690).

Primary (1ry) Antibodies were incubated for one hour and detected using the BOND™ Polymer Refine Detection System (DS9800, Leica Biosystems) as per manufacturer's instructions, substituting the DAB for the Opal fluorophores, with a 10 min incubation time and without the Haematoxylin step. Antigen retrieval at 100 ºC for 20 min, as per standard Leica protocol, with Epitope Retrieval (ER) Solution 2 (AR9640, Leica Biosystems) was performed before each 1ry antibody was applied. Slides were then mounted with VECTASHIELD® Vibrance™ Antifade Mounting Medium with DAPI (H-1800-10, Vector Laboratories. Whole slide scans and multispectral images (MSI) were obtained on the AKOYA Biosciences Vectra® Polaris™. Batch analysis of the MSIs from each case was performed with the inForm 2.4.8 software provided. Finally, batched analysed MSIs were fused in HALO (Indica Labs), to produce a spectrally unmixed reconstructed whole tissue image, ready for analysis.

Cover slips were lifted post multiplex staining and CD68 (Clone PG-M1, Dako M0876) antibody was stained for chromogenically on the Leica BOND autostainer. Antigen retrieval at 100 ºC for 20 min with Epitope Retrieval Solution 2 (AR9640, Leica Biosystems); primary antibody incubation at 1/400 dilution for 30 min then detection using the BOND™ Polymer Refine Detection System (DS9800, Leica Biosystems) as per manufacturer's instructions.

Multiplex immunohistochemistry- Image Analysis

Scanned slides were analysed using Indica Labs HALO® (version 3.0.311.407) image analysis software. Multiplex and brightfield images were manually annotated by a pathologist, defining areas of pancreas, pancreatitis, pancreatic adenocarcinoma and lymph node. The pathologist taught an integrated Random Forrest Classifier module to segment the multiplex images into stroma and epithelium, with obvious areas artefactual staining manually excluded. A separate Random Forest Classifier algorithm was taught to segment tissue into areas of high, medium and low smooth muscle actin (αSMA) expression. Analysis and cell detection/phenotyping was done using Indica Labs - HighPlex FL v3.1.0 (fluorescent images) and Indica Labs – Multiplex IHC v2.1.1 (brightfield images). Cells were annotated based on their marker expression as follows: Epithelium (DAPI+ Cytokeratin+), CD4 helper (DAPI+CD4+), CD8 cytotoxic

(DAPI+CD8+) and regulatory T-cell (DAPI+CD4+Foxp3+). Multiplex and brightfield images were registered and topological analysis was carried out using integrated proximity analysis modules. Proximity analysis was done using a 50 μm with 20 bands cut-off as this allowed us to capture physically interacting cells (within ~ 20 μm radius) as well as account for cells that could contribute to soluble effector molecule gradients. Statistical analysis was done using 2-way ANOVA in Prism (GraphPad).

Single-cell RNA sequencing analysis: Pre-processing, integration and batch correction

FastQ files for 24 PDAC and 11 normal samples were downloaded from the Genome Sequence Archive (https://bigd.big.ac.cn/search?dbId=gsa&q=CRA001160), count matrices were generated in Cell Ranger 3.1.0 as per the original paper (*37*). Raw count matrices were imported into the Seurat R package and merged (*53*). Cells with <200 and >2.5x10^{10} genes, <400 and > 1x10^{16} molecules, and >25% mitochondrial genes were excluded. Batch correction was performed in Harmony (*54*).

Single-cell RNA sequencing analysis: *Single cell clustering and annotation*

Uniform manifold approximation and projection (UMAP) was performed on the scRNAseq harmonised cell embeddings, upon which clustering was performed. 12 broad cell clusters were identified using reference pancreas and immune gene lists (supplemental data 3). The T-cell cluster was subsetted into a new Seurat object, and UMAP was re-performed using genes relevant to T-cells to generate 250 clusters (supplemental table 4).

Mean and 75th percentile normalised count matrices were generated for these clusters. 75th percentile normalised counts were used for cluster identification for all genes except for *CD4* and *B3GAT1* (where, due to low gene capture (*55*) in all clusters, means were used). Clusters without expression of any of *CD3D*, *CD3E*, *CD3G* were excluded to ensure only T-cells were analysed. Double negative clusters were defined by negative 75th percentile expression of *CD8A* and *CD8B*, and negative mean expression of *CD4*. Double positive clusters were defined by positive expression of these genes. The CD4^{+} T-cells were defined as the remaining clusters with positive mean expression of *CD4*. The CD8^{+} T-cells were defined as the remaining clusters which co-express *CD8A* and *CD8B*. The following filters were used for cluster definitions of validated cell populations: Tregs (positive expression of *FOXP3*); Senescent (negative expression of

CD27 and *CD28*, positive 75th percentile expression of *KLRG1* and positive mean expression of *B3GAT1*); Exhausted (positive 75th quantile expression of ≥ 4 of *HAVCR2*, *PDCD1*, *TOX*, *LAG3*, *CTLA4*, *TIGIT*, *CD38*, *ENTPD-1* and positive expression of TRDC was filtered out to exclude gamma-delta T-cells).

Single-cell RNA sequencing analysis: *Data analysis and figures*

Differential expression analysis was performed with the FindMarkers function in Seurat. Scaled expression was extracted from Seurat tumour samples only and truncated violins were plotted with Prism (GraphPad). Normalised expression heatmaps were plotted in Prism (GraphPad) using matrices of 75th percentile and mean expression.

Supplementary Materials

Figure 1- figure supplement 1: Individual patients' immune populations.

Figure 1- figure supplement 2: Individual patients' NK populations.

Figure 1- figure supplement 3: Individual patients' Granulocyte populations.

Figure 1- figure supplement 4: Individual patients' Mononuclear Phagocytes populations.

Figure 1- figure supplement 5: Immune-complexes and MDSC observed in peripheral blood of PDAC patients.

Figure 2- figure supplement 1: Individual patients' CD8^{+} T-cells populations.

Figure 2- figure supplement 2: Individual patients' CD4^{+} T-cells populations.

Figure 2- figure supplement 3: Individual patients' Treg populations.

Figure 2- figure supplement 4: Similar T-cell signatures of senescence and suppression to tumours are observed in peripheral blood.

Figure 2- figure supplement 5: Expression profiles of TIGIT in blood and tumour and cell frequency validation with scRNA seq.

Figure 3- figure supplement 1: Multiplex cell annotation scheme.

Table S1. Patient Data

Table S2. CyTOF Panel

Data File 1: Top differentially expressed genes by 75th percentile and means for Exhausted, Senescent and T-reg metaclusters.

Data File 2: Differential expression analysis for Exhausted, Senescent and T-reg metaclusters.

Data File 3: Reference pancreas and immune gene lists

Data File 4: T-cell complete gene list

References

1. T. Kamisawa, L. D. Wood, T. Itoi, K. Takaori, Pancreatic cancer. *The Lancet* **388**, 73-85 (2016).
2. T. Conroy *et al.*, FOLFIRINOX or gemcitabine as adjuvant therapy for pancreatic cancer. *New England Journal of Medicine* **379**, 2395-2406 (2018).
3. I. De Santiago *et al.*, Immunophenotypes of pancreatic ductal adenocarcinoma: Meta-analysis of transcriptional subtypes. *International journal of cancer*, (2019).
4. Y. Ino *et al.*, Immune cell infiltration as an indicator of the immune microenvironment of pancreatic cancer. *British journal of cancer* **108**, 914-923 (2013).
5. C. E. Clark *et al.*, Dynamics of the immune reaction to pancreatic cancer from inception to invasion. *Cancer research* **67**, 9518-9527 (2007).
6. I. De Santiago *et al.*, Immunophenotypes of pancreatic ductal adenocarcinoma: Meta-analysis of transcriptional subtypes. *International journal of cancer* **145**, 1125-1137 (2019).
7. E. S. Knudsen *et al.*, Stratification of pancreatic ductal adenocarcinoma: combinatorial genetic, stromal, and immunologic markers. *Clinical Cancer Research* **23**, 4429-4440 (2017).
8. L. J. Bayne *et al.*, Tumor-derived granulocyte-macrophage colony-stimulating factor regulates myeloid inflammation and T cell immunity in pancreatic cancer. *Cancer cell* **21**, 822-835 (2012).
9. S. Roth *et al.*, Evolution of the immune landscape during progression of pancreatic intraductal papillary mucinous neoplasms to invasive cancer. *EBioMedicine* **54**, (2020).
10. J. Brahmer *et al.*, Nivolumab versus docetaxel in advanced squamous-cell non–small-cell lung cancer. *New England Journal of Medicine* **373**, 123-135 (2015).
11. C. Robert *et al.*, Pembrolizumab versus ipilimumab in advanced melanoma. *New England Journal of Medicine* **372**, 2521-2532 (2015).
12. M. Aglietta *et al.*, A phase I dose escalation trial of tremelimumab (CP-675,206) in combination with gemcitabine in chemotherapy-naive patients with metastatic pancreatic cancer. *Annals of oncology* **25**, 1750-1755 (2014).
13. G. L. Beatty *et al.*, A phase I study of an agonist CD40 monoclonal antibody (CP-870,893) in combination with gemcitabine in patients with advanced pancreatic ductal adenocarcinoma. *Clinical cancer research* **19**, 6286-6295 (2013).
14. E. M. O'Reilly *et al.*, Durvalumab with or without tremelimumab for patients with metastatic pancreatic ductal adenocarcinoma: a phase 2 randomized clinical trial. *JAMA oncology* **5**, 1431-1438 (2019).
15. K. Young, D. J. Hughes, D. Cunningham, N. Starling, Immunotherapy and pancreatic cancer: unique challenges and potential opportunities. *Ther Adv Med Oncol* **10**, 1758835918816281-1758835918816281 (2018).

16. J. L. Carstens *et al.*, Spatial computation of intratumoral T cells correlates with survival of patients with pancreatic cancer. *Nature communications* **8**, 1-13 (2017).
17. M. Wartenberg *et al.*, Accumulation of FOXP3+ T-cells in the tumor microenvironment is associated with an epithelial-mesenchymal-transition-type tumor budding phenotype and is an independent prognostic factor in surgically resected pancreatic ductal adenocarcinoma. *Oncotarget* **6**, 4190 (2015).
18. A. Popovic, E. M. Jaffee, N. Zaidi, Emerging strategies for combination checkpoint modulators in cancer immunotherapy. *J Clin Invest* **128**, 3209-3218 (2018).
19. K. M. Mahoney, P. D. Rennert, G. J. Freeman, Combination cancer immunotherapy and new immunomodulatory targets. *Nature Reviews Drug Discovery* **14**, 561-584 (2015).
20. S. Pandol, M. Edderkaoui, I. Gukovsky, A. Lugea, A. Gukovskaya, Desmoplasia of Pancreatic Ductal Adenocarcinoma. *Clinical Gastroenterology and Hepatology* **7**, S44-S47 (2009).
21. Y. S. Khaled, B. J. Ammori, E. Elkord, Increased Levels of Granulocytic Myeloid-Derived Suppressor Cells in Peripheral Blood and Tumour Tissue of Pancreatic Cancer Patients. *Journal of Immunology Research* **2014**, 879897 (2014).
22. J. Pillay, T. Tak, V. M. Kamp, L. Koenderman, Immune suppression by neutrophils and granulocytic myeloid-derived suppressor cells: similarities and differences. *Cell Mol Life Sci* **70**, 3813-3827 (2013).
23. S. Singhal *et al.*, Origin and Role of a Subset of Tumor-Associated Neutrophils with Antigen-Presenting Cell Features in Early-Stage Human Lung Cancer. *Cancer Cell* **30**, 120-135 (2016).
24. R. Z. Panni *et al.*, Tumor-induced STAT3 activation in monocytic myeloid-derived suppressor cells enhances stemness and mesenchymal properties in human pancreatic cancer. *Cancer Immunology, Immunotherapy* **63**, 513-528 (2014).
25. B. E. Hsu *et al.*, Immature low-density neutrophils exhibit metabolic flexibility that facilitates breast cancer liver metastasis. *Cell reports* **27**, 3902-3915. e3906 (2019).
26. J. G. Burel *et al.*, Circulating T cell-monocyte complexes are markers of immune perturbations. *Elife* **8**, e46045 (2019).
27. L. Pangrazzi, B. Weinberger, T cells, aging and senescence. *Experimental Gerontology* **134**, 110887 (2020).
28. B. I. Pereira *et al.*, Sestrins induce natural killer function in senescent-like CD8+ T cells. *Nature Immunology* **21**, 684-694 (2020).
29. J. P. Chou, R. B. Effros, T cell replicative senescence in human aging. *Curr Pharm Des* **19**, 1680-1698 (2013).
30. X. Liu, D. F. Hoft, G. Peng, Senescent T cells within suppressive tumor microenvironments: emerging target for tumor immunotherapy. *The Journal of Clinical Investigation* **130**, 1073-1083 (2020).
31. E. Ghorani *et al.*, The T cell differentiation landscape is shaped by tumour mutations in lung cancer. *Nature Cancer* **1**, 546-561 (2020).
32. J. Fourcade *et al.*, CD226 opposes TIGIT to disrupt Tregs in melanoma. *JCI Insight* **3**, (2018).

33. C. A. Fuhrman *et al.*, Divergent Phenotypes of Human Regulatory T Cells Expressing the Receptors TIGIT and CD226. *The Journal of Immunology*, (2015).
34. N. Joller *et al.*, Treg cells expressing the coinhibitory molecule TIGIT selectively inhibit proinflammatory Th1 and Th17 cell responses. *Immunity* **40**, 569-581 (2014).
35. Q. Chen *et al.*, ICOS signal facilitates Foxp3 transcription to favor suppressive function of regulatory T cells. *Int J Med Sci* **15**, 666-673 (2018).
36. M. Vocanson *et al.*, Inducible costimulator (ICOS) is a marker for highly suppressive antigen-specific T cells sharing features of TH17/TH1 and regulatory T cells. *J Allergy Clin Immunol* **126**, 280-289, 289.e281-287 (2010).
37. J. Peng *et al.*, Single-cell RNA-seq highlights intra-tumoral heterogeneity and malignant progression in pancreatic ductal adenocarcinoma. *Cell Res* **29**, 725-738 (2019).
38. O. Khan *et al.*, TOX transcriptionally and epigenetically programs CD8+ T cell exhaustion. *Nature* **571**, 211-218 (2019).
39. C. Zheng *et al.*, Landscape of Infiltrating T Cells in Liver Cancer Revealed by Single-Cell Sequencing. *Cell* **169**, 1342-1356.e1316 (2017).
40. N. Hiraoka, K. Onozato, T. Kosuge, S. Hirohashi, Prevalence of FOXP3⁺ Regulatory T Cells Increases During the Progression of Pancreatic Ductal Adenocarcinoma and Its Premalignant Lesions. *Clinical Cancer Research* **12**, 5423-5434 (2006).
41. Y. Zhang *et al.*, Regulatory T cell depletion alters the tumor microenvironment and accelerates pancreatic carcinogenesis. *Cancer Discovery*, CD-19-0958 (2020).
42. W. J. Ho, E. M. Jaffee, L. Zheng, The tumour microenvironment in pancreatic cancer — clinical challenges and opportunities. *Nature Reviews Clinical Oncology*, (2020).
43. N. G. Steele *et al.*, Multimodal mapping of the tumor and peripheral blood immune landscape in human pancreatic cancer. *Nature Cancer*, 1-16 (2020).
44. L. E. Lucca *et al.*, TIGIT signaling restores suppressor function of Th1 Tregs. *JCI insight* **4**, e124427 (2019).
45. H.-s. Jin *et al.*, CD226^{hi}CD8⁺ T Cells Are a Prerequisite for Anti-TIGIT Immunotherapy. *Cancer Immunology Research*, (2020).
46. H. Sakamoto *et al.*, The Evolutionary Origins of Recurrent Pancreatic Cancer. *Cancer Discovery* **10**, 792-805 (2020).
47. D. Kasakovski, L. Xu, Y. Li, T cell senescence and CAR-T cell exhaustion in hematological malignancies. *J Hematol Oncol* **11**, 91-91 (2018).
48. H. Nakagami, Cellular senescence and senescence-associated T cells as a potential therapeutic target. *Geriatr Gerontol Int* **20**, 97-100 (2020).
49. A. Lanna, S. M. Henson, D. Escors, A. N. Akbar, The kinase p38 activated by the metabolic regulator AMPK and scaffold TAB1 drives the senescence of human T cells. *Nature Immunology* **15**, 965-972 (2014).
50. Y. Zhao, Q. Shao, G. Peng, Exhaustion and senescence: two crucial dysfunctional states of T cells in the tumor microenvironment. *Cellular & Molecular Immunology* **17**, 27-35 (2020).

51. X. Liu *et al.*, Regulatory T cells trigger effector T cell DNA damage and senescence caused by metabolic competition. *Nature Communications* **9**, 249 (2018).
52. M. Huber *et al.*, The Immune Microenvironment in Pancreatic Cancer. *International Journal of Molecular Sciences* **21**, 7307 (2020).
53. A. Butler, P. Hoffman, P. Smibert, E. Papalexi, R. Satija, Integrating single-cell transcriptomic data across different conditions, technologies, and species. *Nature Biotechnology* **36**, 411-420 (2018).
54. I. Korsunsky *et al.*, Fast, sensitive and accurate integration of single-cell data with Harmony. *Nature Methods* **16**, 1289-1296 (2019).
55. C. Yang *et al.*, Heterogeneity of human bone marrow and blood natural killer cells defined by single-cell transcriptome. *Nature Communications* **10**, 3931 (2019).

Acknowledgments:

We thank all members of the Dustin lab for fruitful discussions. We thank Vincenzo Cerundolo and Giorgio Napolitano for discussions on CyTOF panel design. We thank A. Lanna for helpful discussion on senescent T-cells. We thank A. van der Merwe, A. Artzy-Schinrman, A. Morch and P. Cespedes for comments on the manuscript. We thank L. Campo and the translation histopathology lab for help with multiplex IHC imaging. We thank S. Jones and Oxford Research Biobank for help with tissue cutting and collection. We acknowledge the contribution to this study made by the Oxford Centre for Histopathology Research and the Oxford Radcliffe Biobank, which are supported by the NIHR Oxford Biomedical Research Centre.

Funding

A national institute for health research (NIHR) academic clinical lectureship supported SS for the majority of this work. Oxford human immunology discovery initiative, cancer research UK and LAP (liver and pancreas fund) supported SS. SS is now supported by a career development fellowship from BMS. An UCB-Oxford Post-doctoral Fellowship supported EAS. MRM is supported by the NIHR Oxford Biomedical Research Centre. The views expressed are those of the authors and not necessarily those of the NIHR or the Department of Health and Social Care. Wellcome

Trust Principal Research Fellowship 100262Z/12/Z and a grant from KTRR supported M.L.D.

Author's Contributions

Conceptualisation: SS, EAS, MRM, MLD. *Investigation*: SS, EAS. *Methodology*: SS, EAS, JA, AE, EHAB, RBR. *Visualisation*: EAS, EHAB. *Formal analysis*: EAS, EHAB, RBR, DJA, LRH. *Data curation*: SS, EAS, DJA, EHAB, AE. *Project administration*: SS, EAS. *Resources*: NM, SR, AR, EK, MS. *Funding acquisition*: SS, EAS, MRM, MLD. *Writing - original draft*: EAS, SS. *Writing - review & editing:* everyone. *Supervision*: MRM, MLD.

Competing interests

SS has salary and expenses from BMS in the form of a career development fellowship. RJMB-R is a co-founder and consultant for Alchemab Therapeutics Ltd and a consultant for Imperial College London and VHSquared. MM reports personal fees from Amgen, grants and personal fees from Roche, grants from Astrazeneca, grants and personal fees from GSK, personal fees and other from Novartis, other from Millenium, personal fees, non-financial support and other from Immunocore, personal fees and other from BMS, personal fees and other from Eisai, other from Pfizer, personal fees, non-financial support and other from Merck/MSD, personal fees and other from Rigontec (acquired by MSD), other from Regeneron, personal fees from BiolineRx, personal fees and other from Array Biopharma (now Pfizer), non-financial support and other from Replimune, personal fees from Kineta, personal fees from Silicon Therapeutics, outside the submitted work. All other authors have no relevant conflicts of interest to declare.

Data Availability

Data available upon reasonable request from authors.

A

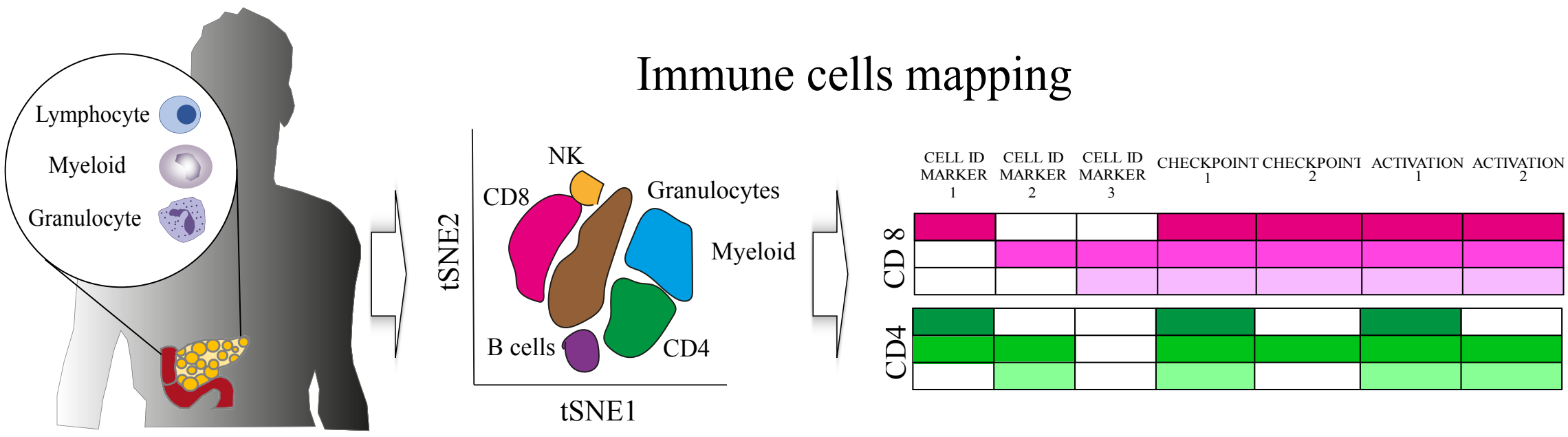

B

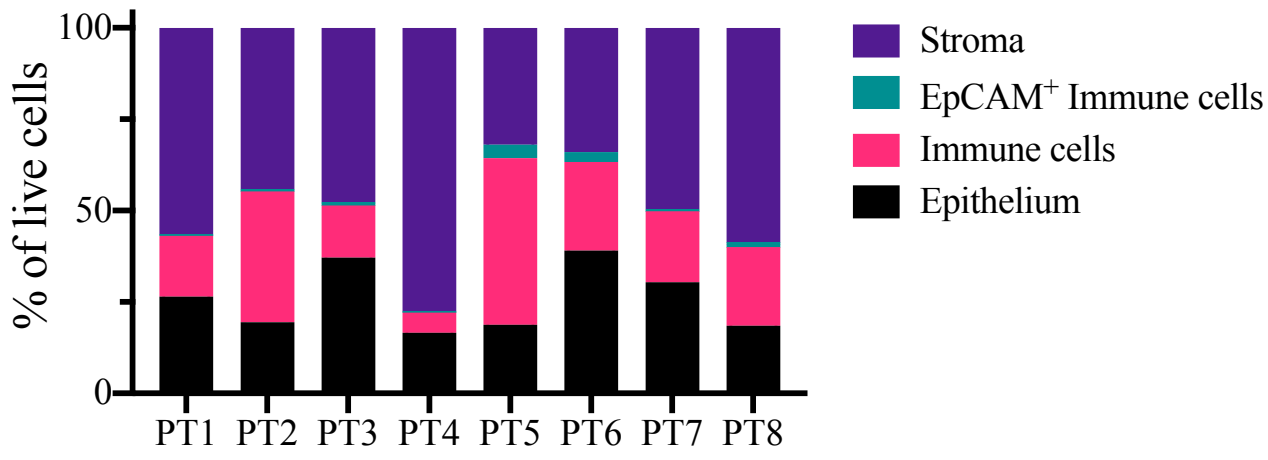

C

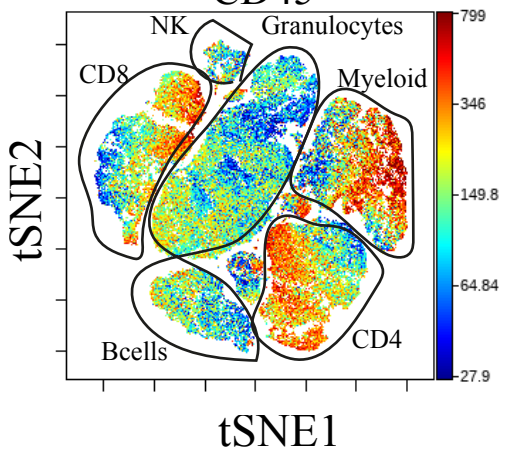

D

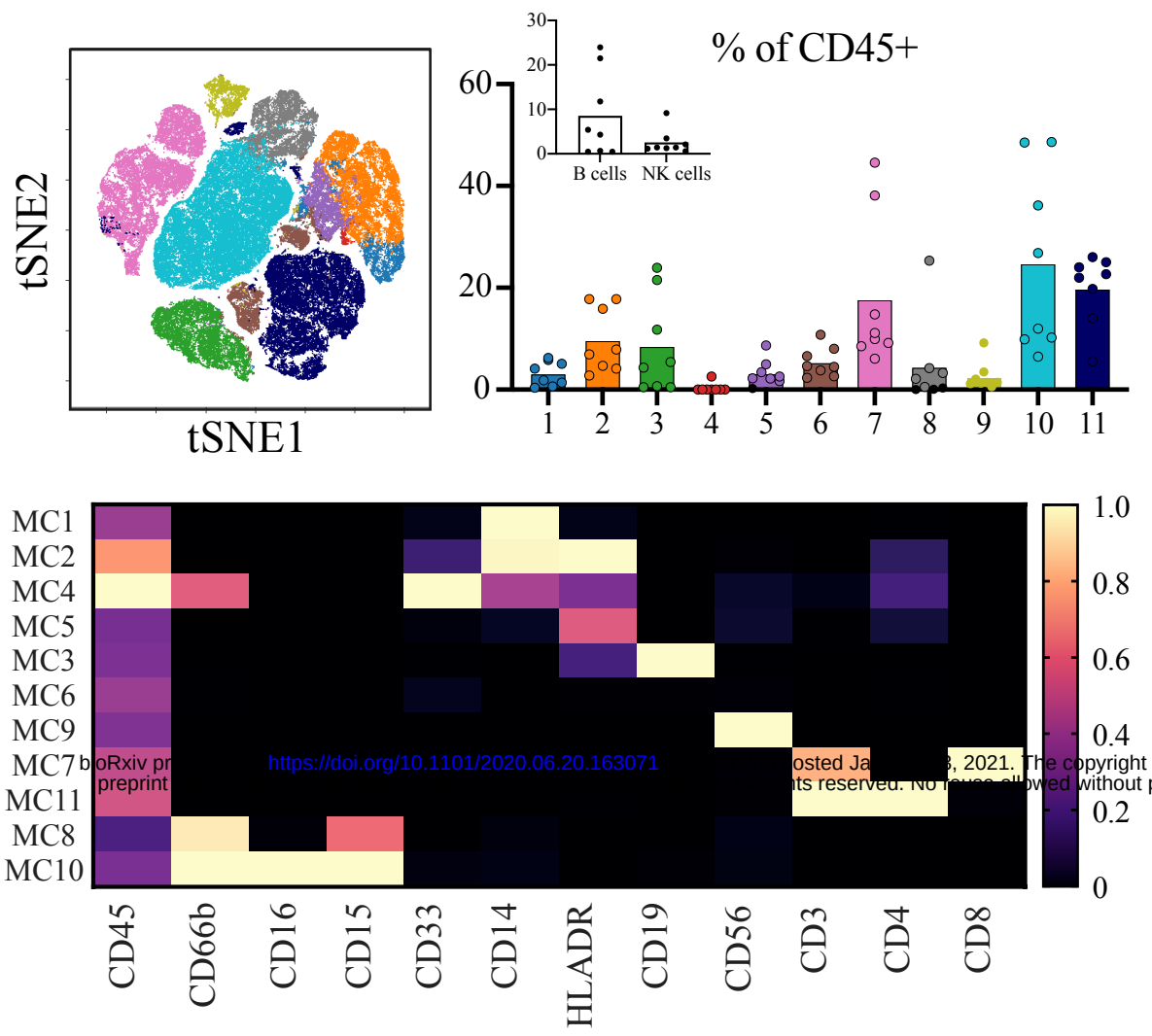

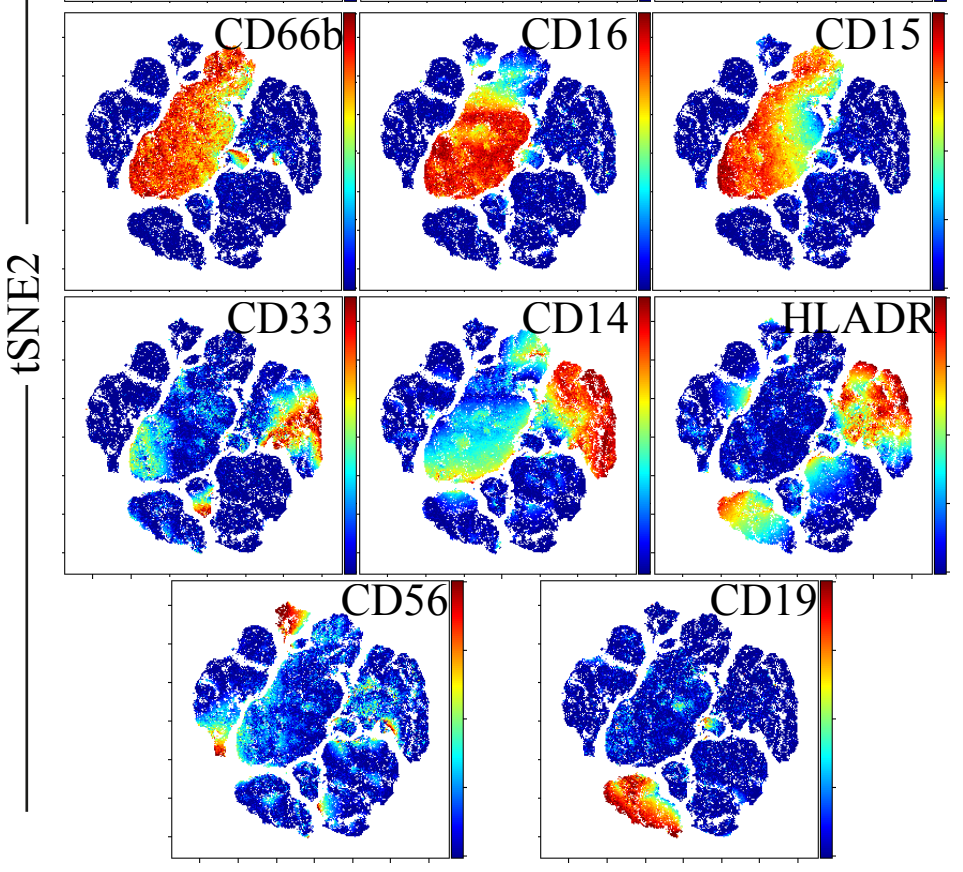

E

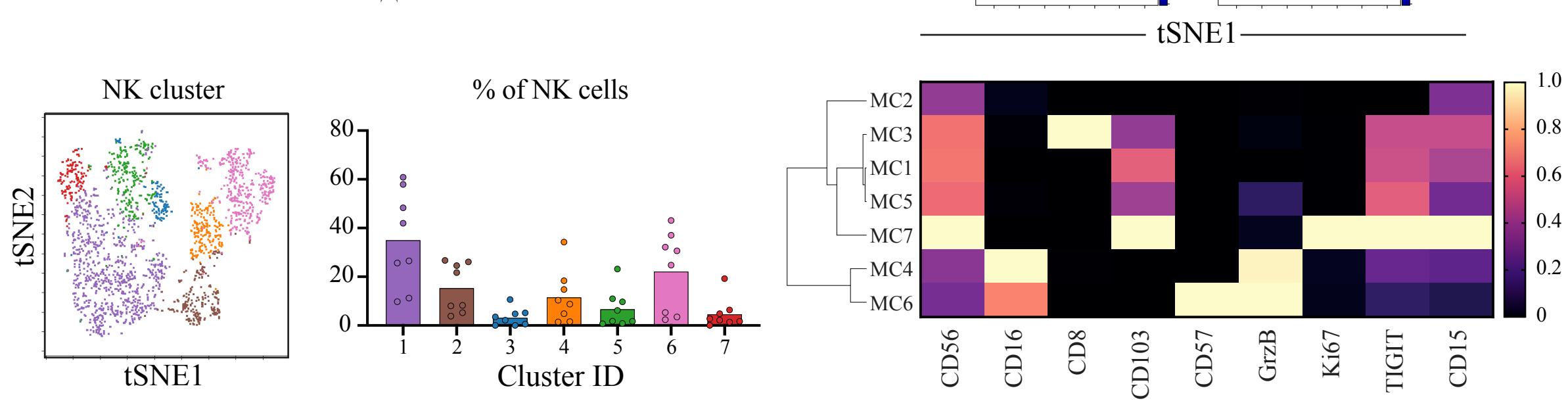

F

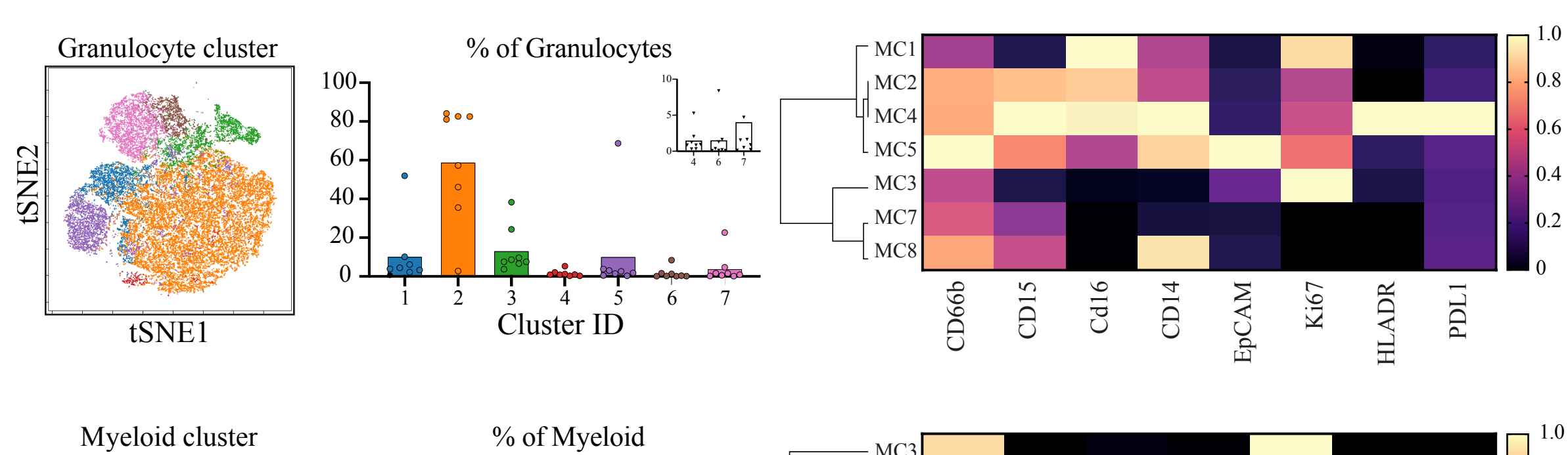

G

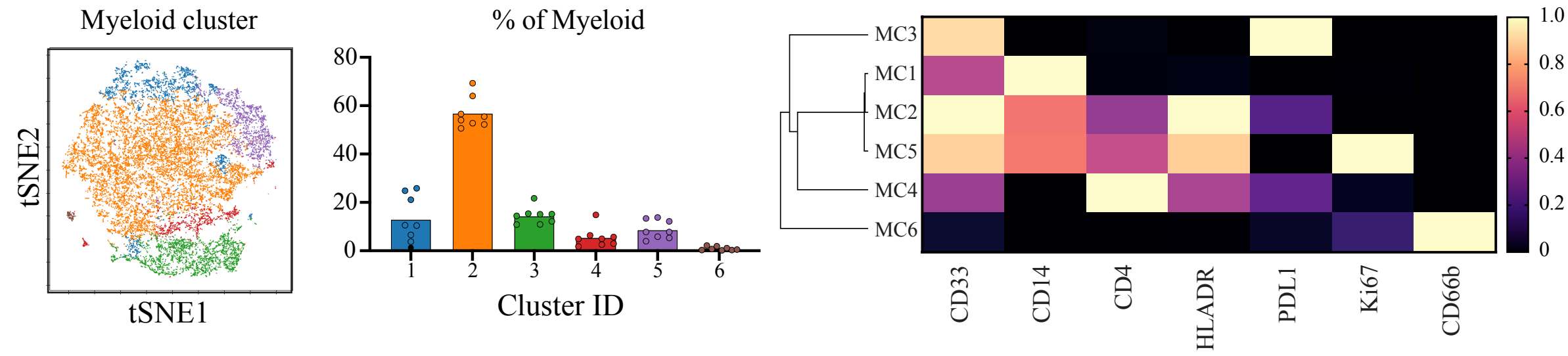

Figure 1, Sivakumar and Abu-Shah et al

Figure 1: Immune infiltration into PDAC is heterogenous but with a marked T-cell population. (A) Schematics of the experimental procedure; primary resectable pancreatic tumours are made into single-cell suspensions and taken for phenotyping using mass cytometry (CyTOF). CyTOF data was clustered using cytobank FlowSOM to identify common populations across patients. Using a set of lineage markers, checkpoints and activation markers cellular states and functionality are defined with a focus on T-cell populations. (B) 200,000 cells pooled from 8 patients were gated in silico and cellular granularity was assessed; Immune cells ($CD45^+$), epithelial cells ($EpCAM^+$), Stroma ($CD45^-EpCAM^-$) and EpCAM+ Immune cells ($CD45^+EpCAM^+$). (C) 100,000 $CD45^+$ cells pooled from 8 patients and viSNE analysis using main cell lineage markers was performed to identify the main immune cell populations. viSNE plot is shown with manual annotation of cell identities (top), expression profile of the CyTOF markers used for clustering is shown (bottom). (D) viSNE plot of the main immune populations coloured and labelled by FlowSOM. Bar plots of metacluster frequencies in each patient. Inset shows the B-cell and NK clusters (CV %111.3 and 108.6% respectively). Heatmap of FlowSOM metaclusters of $CD45^+$ cells; rows represent metaclusters from combined single cells across patients. (E) NK cells were clustered with FlowSOM and 7 different metaclusters identified. Metacluster's relative frequency is presented in the bar plot. Inset shows the lower frequency metaclusters. Expression profile for each metacluster is shown in the heatmap (right). The major metacluster being a $CD8^+$ NK population. (F) Granulocyte were clustered with FlowSOM and 7 different metaclusters identified. Metacluster's relative frequency is presented in the bar plot. Inset shows the lower frequency metaclusters. Expression profile for each metacluster is shown in the heatmap (right). The major metacluster expressing an intermediate level of CD16 and CD15. (G) Myeloid cells were clustered

with FlowSOM and 6 different metaclusters identified. Metacluster's relative frequency is presented in the bar plot. Inset shows the lower frequency metaclusters. Expression profile for each metacluster is shown in the heatmap (right). The major metacluster expressing an intermediate level of CD14 and CD33 but high for MHCII (HLA-DR), and another important metacluster is the one lacking HLA-DR expression (MSDC). All bar plots are median and the individual dots are individual patients. Heatmaps are normalised for each marker with lowest expression marked in dark blue as zero, and highest in yellow as 1. MC= metacluster.

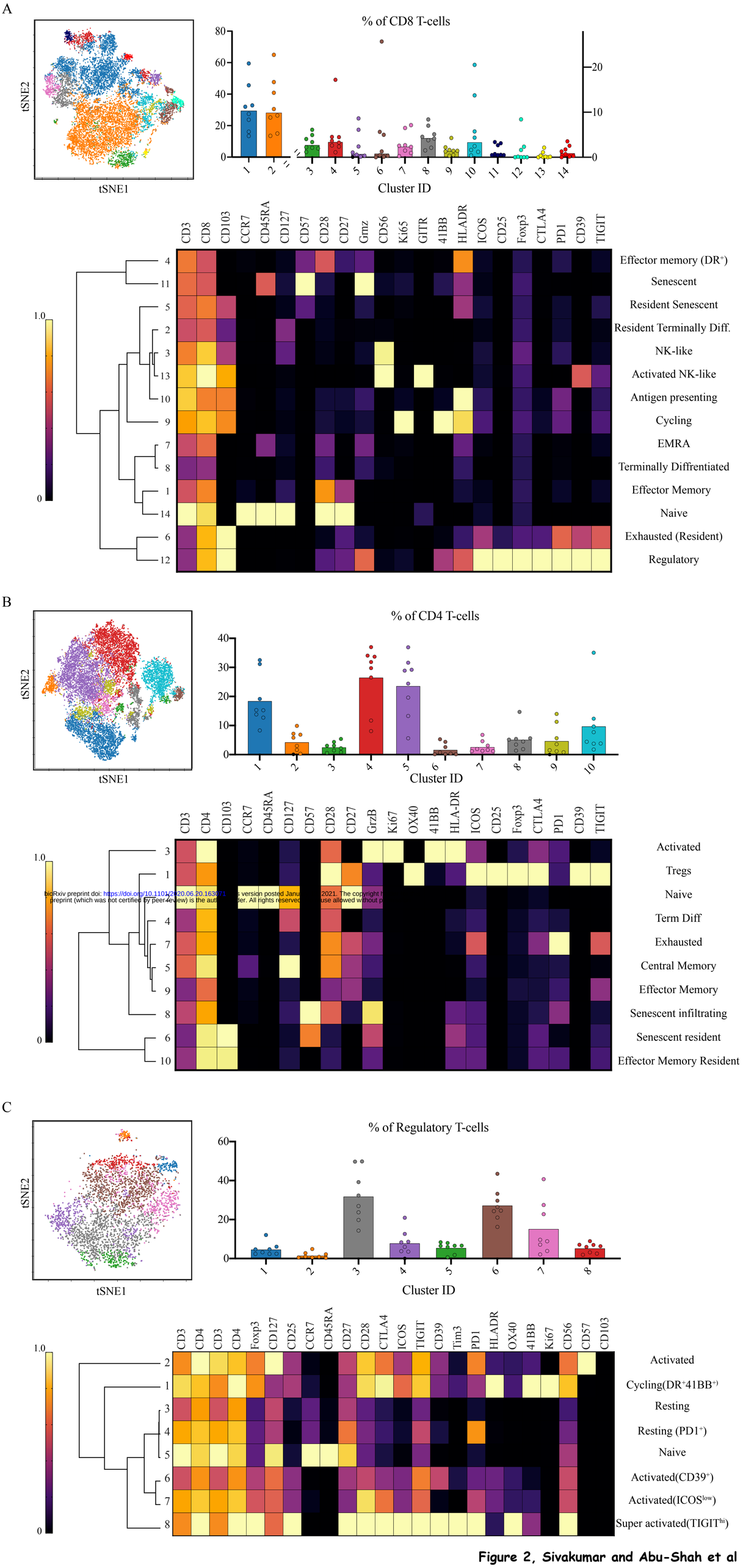

Figure 2, Sivakumar and Abu-Shah et al

Figure 2: $CD8^+$ T-cell senescence and activated Tregs dominate the landscape of the tumour. (A) ~14,750 $CD8^+$ T-cells were pooled and 14 metaclusters identified with FlowSOM and visualised on viSNE plot. Metaclusters' relative abundance is shown in the bar plot MC1,2 are plotted on the left y-axis, MC3-14 are plotted on the right y-axis). The heatmaps show the expression profile of immune checkpoints in the different metaclusters and identified unique populations based on the combinatorial expression. Note that the major $CD8^+$ populations are effector memory cells and the presence of 4 metaclusters corresponding to senescent cells. There is also a proportion of exhausted cells as well as metaclusters of activated cells. (B) ~17,870 $CD4^+$ T-cells were pooled and 10 metaclusters identified with FlowSOM and visualised on viSNE plot. Metaclusters' relative abundance is shown in the bar plot. The heatmaps show the expression profile of immune checkpoints in the different metaclusters and identified unique populations based on the combinatorial expression. The major populations are central memory cells, and there were 5 metaclusters identified as regulatory T-cell (analysed in depth in (C)). (C) ~3,900 $CD4^+$ regulatory T-cells were pooled and 8 metaclusters identified with FlowSOM and visualised on a viSNE plot. Metaclusters' relative abundance is shown in the bar plot. The heatmaps show the expression profile of immune checkpoints in the different metaclusters and identified unique populations based on the combinatorial expression. More than 50% of the metaclusters show an activated phenotype albeit at different magnitudes. All bar plots are median and the individual dots are individual patients. Heatmaps are normalised for each marker with lowest expression marked in dark blue as zero, and highest in yellow as 1. Hierarchal clustering of heatmaps was done in Morpheus.

A

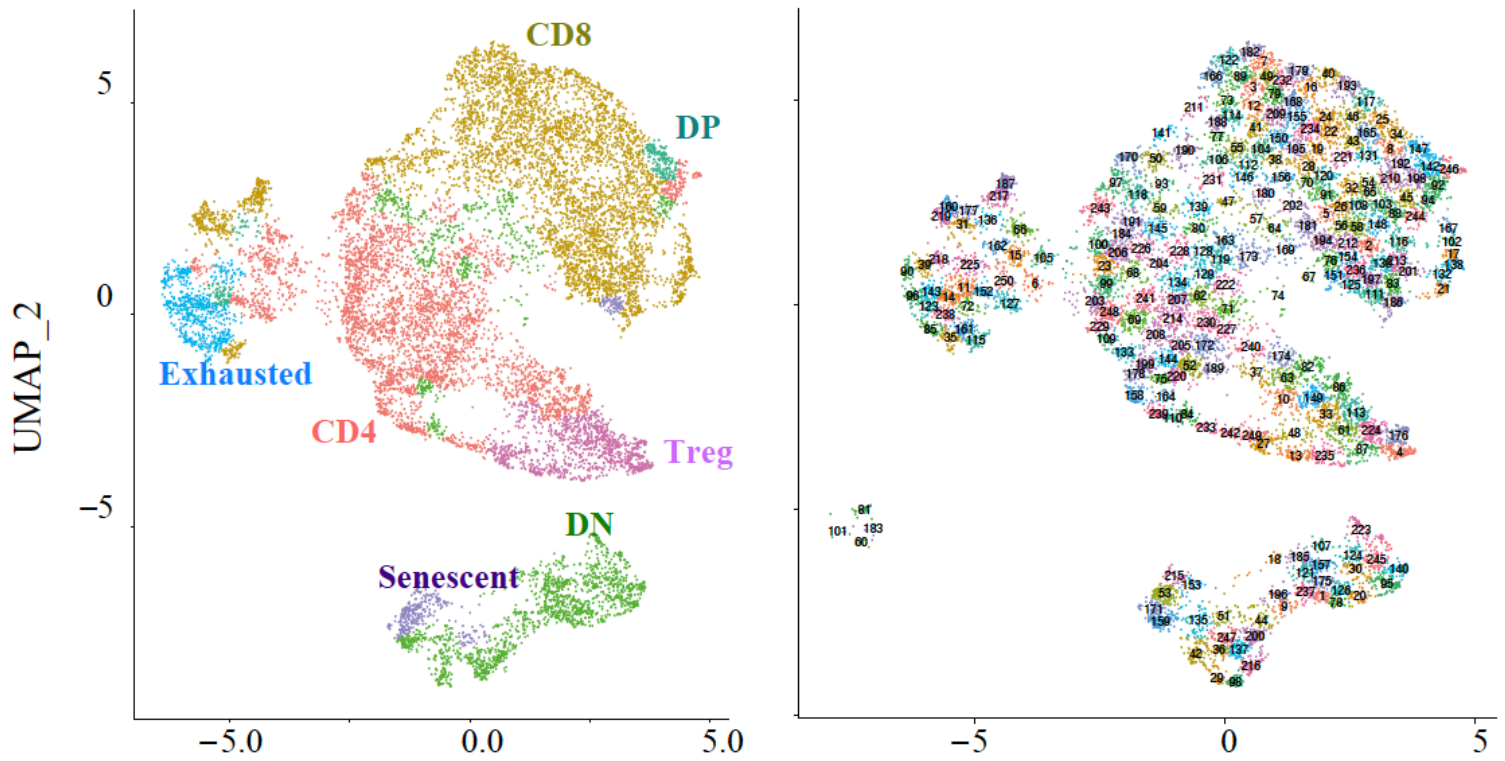

B

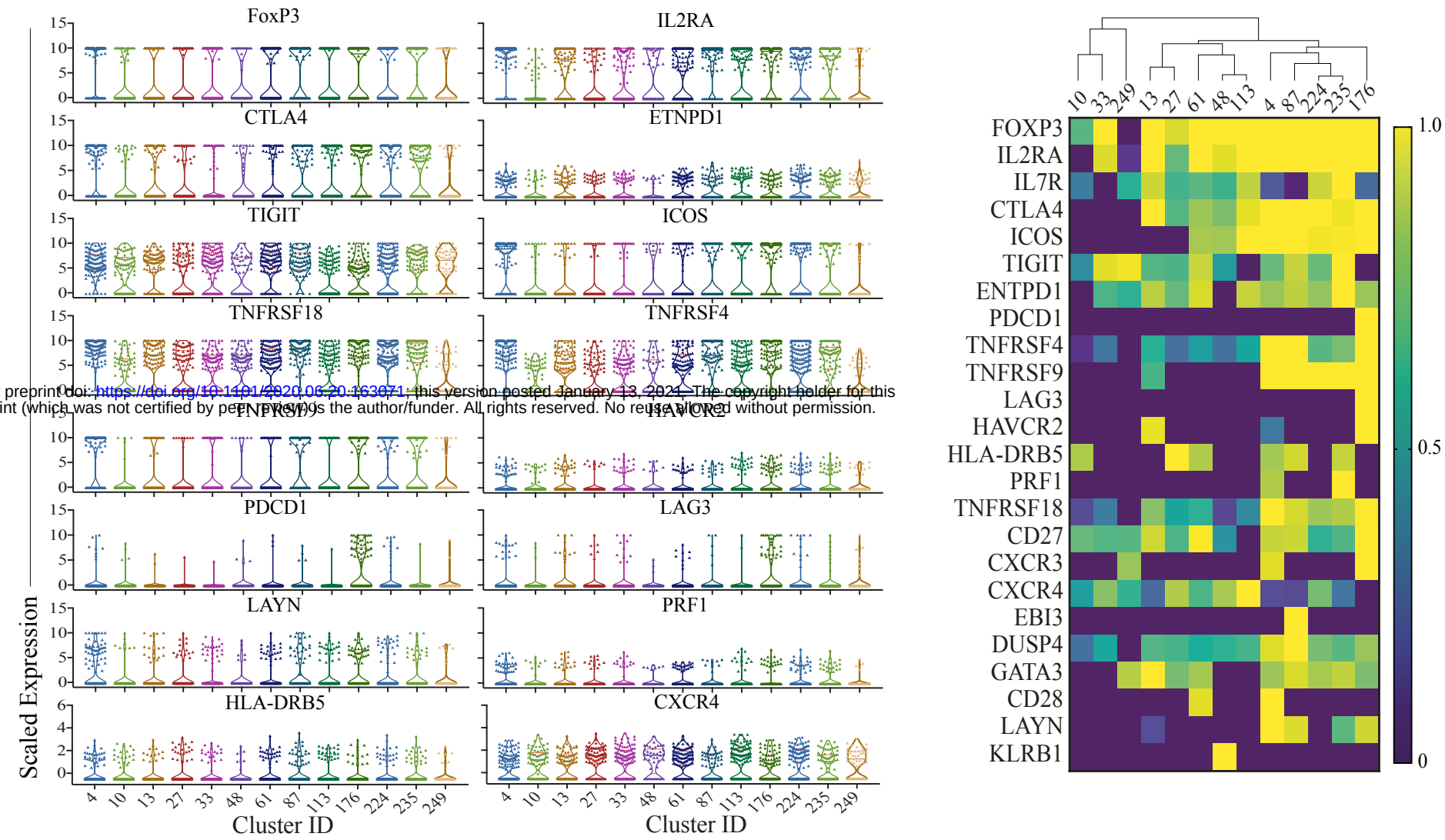

C

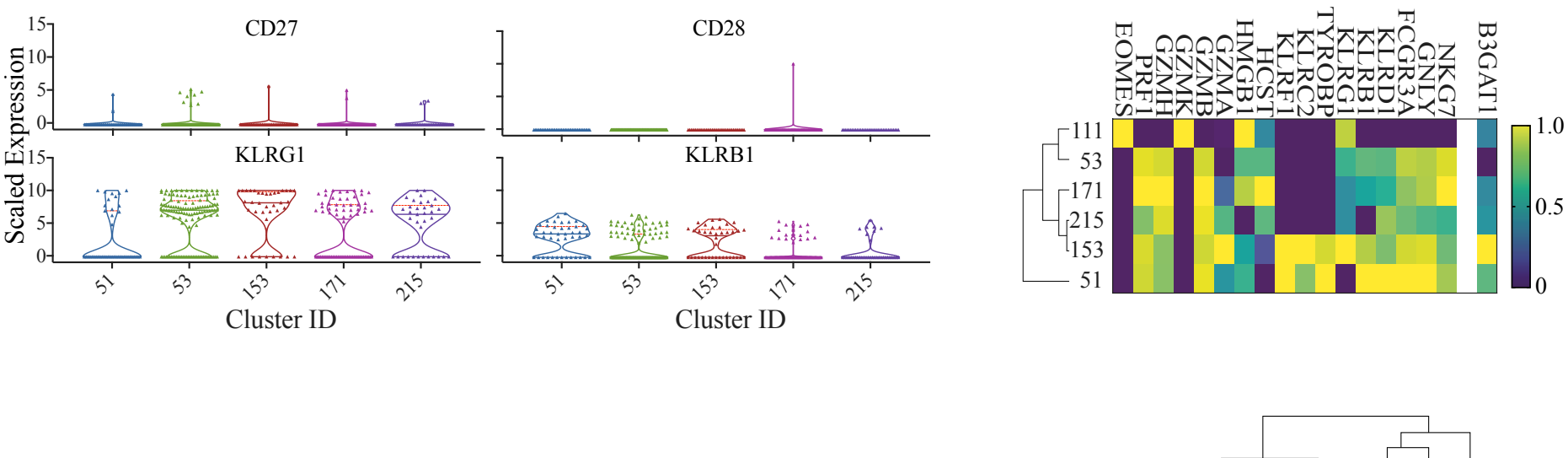

D

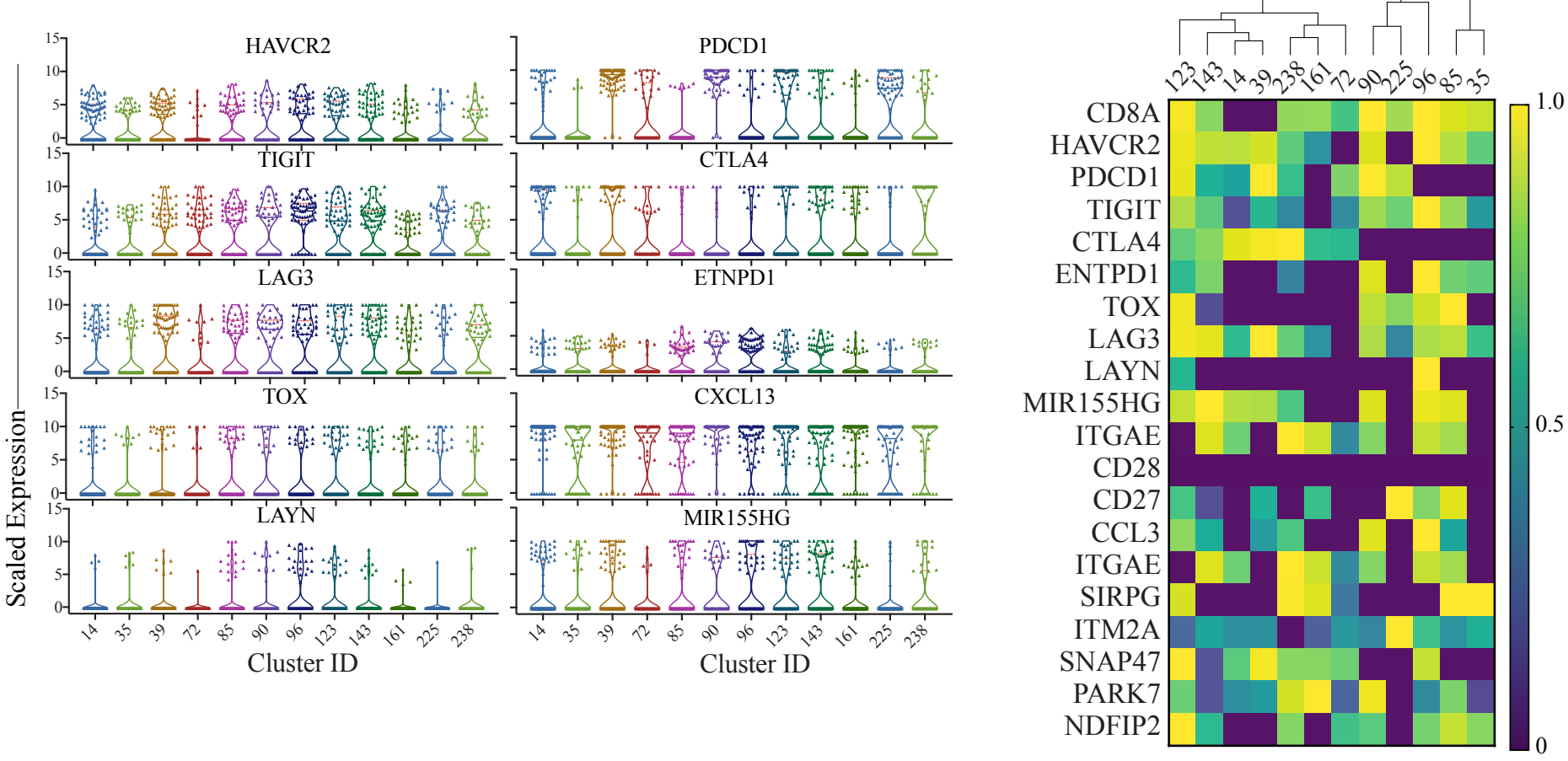

Figure 3, Sivakumar and Abu-Shah et al

Figure 3: Single Cell RNA sequencing reveals senescence and regulatory signature of T-cells. (A) Left, ~13,600 T cells in tumour are projected on UMAP and clusters annotated by the major compartments including regulatory T-cell (pink), senescent T-cells (purple) and exhausted T-cells (cyan). Right, UMAP of the cluster identities in each of the major subsets. (B) Left, Violin plots depicting the 75th percentile scaled expression of the marker genes in the Treg clusters. Right, heatmaps showing the top differentially expressed genes in the Treg clusters. Expression has been normalised per gene. (C) Left, Violin plots of the 75th percentile expression of the key gene signature for the senescent population. Right, Heatmaps showing NK and senescence genes uniquely expressed in the senescent population. Heatmap scale for *B3GAT1* is presented as mean values per cluster rather than the 75th percentile due to low capture of this gene. (D) Left, Violin plots of the 75th percentile expression of the key gene signatures for the exhausted T-cell population. Right, the corresponding heatmaps of the key gene signatures. Full expression profiles per cluster are provided in supplemental data file 2.

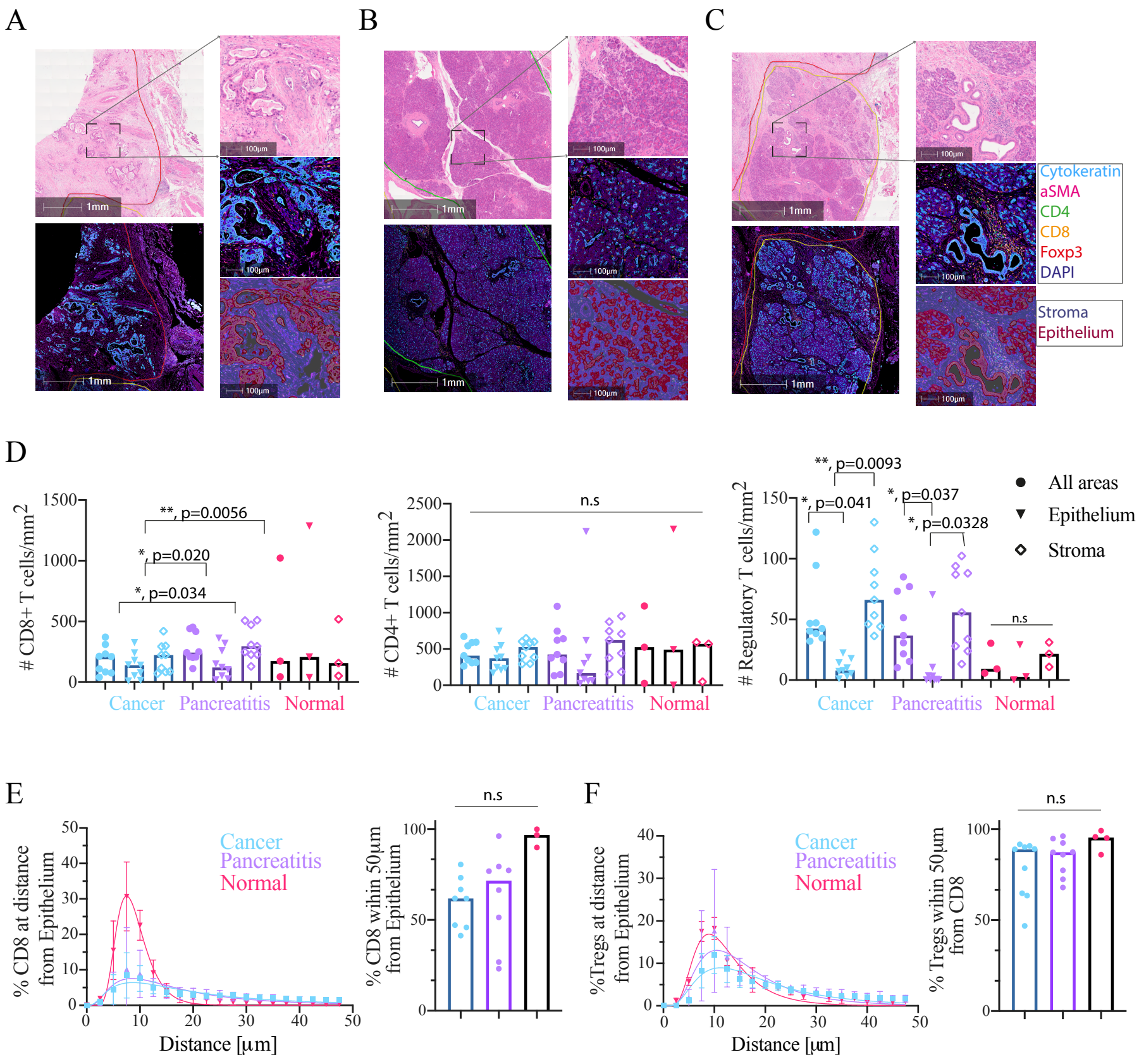

Figure 4, Sivakumar and Abu-Shah et al

Figure 4: Multiplex imaging of T-cell distribution within PDAC tumours identifies a stroma restricted Treg compartment. (A) 2x magnification (left) of a cancer region showing H&E (top) and immunofluorescence (bottom). 10x magnification (right) of a region from (left) showing H&E staining (top), the fluorescence signal (middle) and the region classification into epithelium and stroma (bottom). (B) As in (A) for a pancreatitis region. (C) As in (A) for a normal pancreas. (D) Infiltration of $CD8^+$ T-cells (left), $CD4^+$ T-cells (middle) and Tregs (right) into the tissue (Cancer, Pancreatitis and Normal), as well as sub-tissue architectural distribution between the epithelium-rich and stroma-rich areas. Mixed-effect ANOVA with Tukey's correction. (E) Proximity analysis of $CD8^+$ T-cells distance distribution within 50 μm of epithelial cells fitted using a lognormal distribution with geometric means and R^2 as follows: Cancer: 17.21 μm, 0.80; Pancreatitis 14.55 μm, 0.79; Pancreas: 8.46 μm, 0.99. (F) Proximity analysis of Treg distance distribution within 50 μm of $CD8^+$ T-cells, fitted using a lognormal distribution with geometric means and R^2 as follows: Cancer: 16.75 μm, 0.84; Pancreatitis 14.28 μm, 0.82; Pancreas: 11.24 μm, 0.92.